Modulating Carrier Kinetics in BiVO4 Photoanodes through Molecular Co4O4 Cubane Layers

Chen, Hang ; Li, Jingguo ; Meng, Lingshen ; Bae, Sanghyun ; Erni, Rolf ; Abbott, Daniel F ; Li, Shangkun ; Triana, Carlos A ; Mougel, Victor ; Patzke, Greta R

DOI: https://doi.org/10.1002/adfm.202307862

ADVANCED FUNCTIONAL MATERIALS
www.afm-journal.de

Modulating Carrier Kinetics in $BiVO_4$ Photoanodes through Molecular Co_4O_4 Cubane Layers

Hang Chen, Jingguo Li, Lingshen Meng, Sanghyun Bae, Rolf Erni, Daniel F. Abbott, Shangkun Li, Carlos A. Triana, Victor Mougel, and Greta R. Patzke**

Understanding the role and immobilization of molecular catalysts on photoelectrodes is essential to use their full potential for efficient solar fuel generation. Here, a $Co^{II}_4O_4$ cubane with proven catalytic performance and an active H_2O—$Co_2(OR)_2$—OH_2 edge-site moiety is immobilized on $BiVO_4$ photoanodes through a versatile layer-by-layer assembly strategy. This delivers a photocurrent of 3.3 mA cm^{-2} at 1.23 V_{RHE} and prolonged stability. Tuning the thickness of the Co_4O_4 layer has remarkable effects on photocurrents, dynamic open circuit potentials, and charge carrier behavior. Comprehensive-time and frequency-dependent perturbation techniques are employed to investigate carrier kinetics in transient and pseudo-steady-state operando conditions. It is revealed that the Co_4O_4 layer can prolong carrier lifetime, unblock kinetic limitations at the interface by suppressing recombination, and enhance charge transfer. Additionally, its flexible roles are identified as passivation/hole trapping/catalytic layer at respective lower/moderate/higher potentials. These competing functions are under dynamic equilibrium, which fundamentally defines the observed photocurrent trends.

1. Introduction

Photoelectrochemical (PEC) water splitting on semiconductor electrodes has been attracting tremendous interest as a potential route to store solar energy in the form of renewable fuels, such as hydrogen.[1] However, the thermodynamically and kinetically sluggish multi-electron and multi-proton transfer processes involved in the oxygen evolution reaction (OER) remain challenges on the way to efficient overall water splitting.[2] Bismuth vanadate ($BiVO_4$), an n-type semiconductor, has emerged as a promising candidate for visible-light-assisted oxygen evolution from water,[3] since Kudo et al. first reported on the water oxidation activity of $BiVO_4$ powder in 1998.[4] However, unmodified $BiVO_4$ exhibits poor water oxidation kinetics due to its low electron mobility (weak electronic coupling between V 3d orbitals and Bi 6p orbitals at the conduction band minimum),[5] moderate hole diffusion length (≈70 nm),[6] and detrimental surface electron–hole recombination.[7] Therefore, various strategies have been pursued to alleviate the mobility, lifetime, and kinetic limitations of photogenerated charge carriers, such as defect engineering to accelerate charge transport,[8] surface modification to passivate recombination,[9] and catalyst layer deposition to enhance charge transfer.[10]

Notably, understanding the charge carrier kinetics at the semiconductor–electrolyte interface (SEI) is of paramount importance in photoelectrode design.[11] The authentic role of co-catalysts on the surface photoelectrodes is still controversial due to the complex kinetics of charge carriers at the SEI. Based on intensity-modulated photocurrent spectroscopy (IMPS) and photoinduced absorption spectroscopy results, some studies reported that cocatalysts, such as cobalt phosphate (CoPi) or ferrihydrite, mainly passivated surface recombination of $BiVO_4$ rather than to improve charge transfer and hence photocurrents.[7,12] However, Hamann et al. resolved the role of CoPi cocatalysts as reservoirs withdrawing photogenerated holes from hematite through photoelectrochemical impedance spectroscopy (PEIS) and transient photocurrent spectroscopy (TPS).[13] Along these lines, Durrant et al. proposed that water oxidation is driven by oxidized states within the Ni—Fe oxyhydroxide catalyst layer on $BiVO_4$ photoanodes.[14] Alternatively, for Prussian blue

H. Chen, J. Li, L. Meng, S. Bae, S. Li, C. A. Triana, G. R. Patzke
Department of Chemistry
University of Zurich
CH-8057 Zurich, Switzerland
E-mail: jingguo.li@kemi.uu.se; greta.patzke@chem.uzh.ch
J. Li
Department of Chemistry
Ångström Laboratory
Uppsala University
75120 Uppsala, Sweden
R. Erni
Electron Microscopy Center
Empa
Swiss Federal Laboratories for Materials Science and Technology
CH-8600 Dübendorf, Switzerland
D. F. Abbott, V. Mougel
Department of Chemistry and Applied Biosciences
ETH Zurich
CH-8093 Zurich, Switzerland

The ORCID identification number(s) for the author(s) of this article can be found under https://doi.org/10.1002/adfm.202307862

DOI: 10.1002/adfm.202307862

(CoFe—PB) decorated $BiVO_4$ films, CoFe—PB was proposed as a true catalyst, even though the suppression of surface recombination at the SEI was not ruled out.[15] Moreover, Durrant and coworkers observed a fast and largely irreversible hole transfer in the pre-ms time scale from $BiVO_4$ to CoFe—PB at low bias by employing transient absorption spectroscopy (TAS).[16] This indicated that the OER process was kinetically promoted by the storage of reactive holes in cocatalysts and their subsequent transfer. Despite the achievements in the mechanistic understanding of heterogeneous cocatalysts on photoanodes, few studies elaborately interpret the role of molecular cocatalysts with comprehensive techniques that study the carrier kinetics from a dynamic (TPS) or pseudo-steady-state (PEIS/IMPS) perspective. Moreover, IMPS provides more direct kinetic information regarding the catalytic interface by modulating the surface concentration of the photo-generated carriers than PEIS. Thus, for a detailed analysis of the kinetic processes in a specific scenario, the combination of these techniques is essential.

Recently, promising OER performance has been achieved with molecular catalysts by exploiting their tunable coordination environments around the active sites as a major asset.[17] To apply these advantages of molecular catalysts in PEC systems, various heterogenization strategies have been employed, including physisorption, physical entrapment, and covalent/non-covalent binding.[18] For instance, Co_4O_4 cubanes were immobilized on $BiVO_4$ surfaces via physisorption and hydrophobic interaction by integrating a C_4 alkyl chain into the cubane as the binding group.[19] For physical entrapment, molecular catalysts were embedded in polymeric matrices, such as Nafion,[20,21] but its strongly acidic head groups (—SO_3H) were detrimental to the improvement of photocurrent densities and the minimization of overpotentials. Covalent binding always required sophisticated procedures to design anchoring groups (—PO_3H_2 or —COOH) for molecules or electrodes.[22,23] Non-covalent binding methods were limited to special circumstances, for example, π–π stacking requires that conjugated macrocyclic electron structures are present in both molecules and electrode surfaces.[24] The versatile layer-by-layer (LBL) assembly strategy has been applied with significant success to functionalize solid surfaces via physical, chemical, or coordination chemistry interactions for various applications.[25] Especially for PEC water splitting, this method showed great potential to immobilize cocatalysts,[26] such as polyoxometalate (POM) clusters,[27,28] metal–organic frameworks,[29] and CdX (X = Se, Te, S) quantum dots.[30]

Inspired by the OER center of nature's photosystem II, an artificial Mn_4CaO_5 cluster has been synthesized with analogous active metal sites and shown to be a potential water oxidation catalyst.[31] Alternatively, transition-metal-based (Mn/Co/Ni) cubanes are of great interest as template systems for photochemical OER.[32] Previously, we have reported on a stable and efficient Co_4O_4 cubane $[Co^{II}_4(dpy\{OH\}O)_4(OAc)_2(H_2O)_2](ClO_4)_2$ molecular catalyst for the OER with a reactive $\{H_2O—Co_2(OR)_2—OH_2\}$ edge-site motif.[33] Particularly, our group resolved the role of $\{Co(II)_4O_4\}$-type cocatalysts on hematite films and found that they dynamically changed their role from predominant hole reservoirs to catalytic centers along with the modulation of the applied bias.[21] Here, instead of weakly binding the molecular cubane via simple adsorption,[34,35] we employed the LBL assembly method, as a "click" chemistry approach to build a conformal cubane layer with a tunable thickness and homogeneous Co_4O_4 distribution on $BiVO_4$ photoanodes, as shown in Scheme S1 (Supporting Information). The cubane layer significantly improved the photostability of $BiVO_4$ through the protection of the surface against vanadium dissolution or photocorrosion by rapidly transferring accumulated holes in $BiVO_4$ toward the water oxidation process. We elucidated how the cubane layer enhanced OER performance over a broad range of experimental conditions. In general, modification with Co_4O_4 layers prolongs the lifetime of charge carriers. Specific functions of the cubane layer were furthermore identified, for example how a thin Co_4O_4 layer enables direct hole tunneling for water oxidation. Interestingly, potential-dependent cubane functions were observed with moderate surface loading, namely surface passivation at lower potentials, hole reservoirs at moderate potentials, and active catalysts at higher potentials. Instead of simply binding cobalt cubanes using Nafion on hematite photoanodes,[21] this study provides a more versatile method to immobilize molecules. This enabled us to investigate the general role of molecular cocatalysts comprehensively with a wider range of analytical techniques. Our results offer new strategies for the rational immobilization of functional molecules and provide a clear understanding of the carrier kinetics at the SEI for the design of efficient photoelectrodes.

2. Results and Discussion

2.1. Immobilization and Characterization of Cobalt Cubanes on $BiVO_4$ Photoanodes

The Co_4O_4 cubane was prepared following a previous synthetic protocol reported by some of us.[33] The validity of the molecular structure was confirmed using X-ray diffraction (XRD) and infrared (FT-IR) spectroscopy, as shown in Figures S1,S2 (Supporting Information). The cubane was assembled on $BiVO_4$ photoanodes with tuned thickness using a LBL process as shown in Scheme S1 and Section 1 (Supporting Information). The binding forces to anchor the molecular cubane on PAA-modified $BiVO_4$ electrodes can be attributed both to electrostatic interactions and physical absorptions, as depicted in the introduction. UV/vis spectra showed that the cubane molecule is stable during the LBL assembly process and after continuous aging for ≈36 h (Figure S3, Supporting Information). Interestingly, the absorption of $Co_4O_4/BiVO_4$ films was gradually enhanced, especially in the UVA region (300–400 nm), by increasing the number of assembled layers to 12, as shown in Figure S4 (Supporting Information). Since the ligand-to-metal charge transfer primarily accounts for the observed absorption, it can be deduced that there is an electronic interaction between Co_4O_4 and $BiVO_4$, resulting in the absorption of more photons and the conversion of these photons into free charge carriers in $BiVO_4$. A further increase of the assembled layers only promotes the absorption at ≈400–475 nm but weakens the absorption in the UVA region. This indicates that thick cubane layers hinder the absorption of light in the UVA region for $BiVO_4$ due to the loss of photons in the cubane layer. However, the increased concentration, with an absorption range from ≈425–600 nm (Figure S3, Supporting Information), is responsible for the extended absorption at ≈400–475 nm and the out-of-band absorption (≈480–600 nm) for $Co_4O_4/BiVO_4$ films.

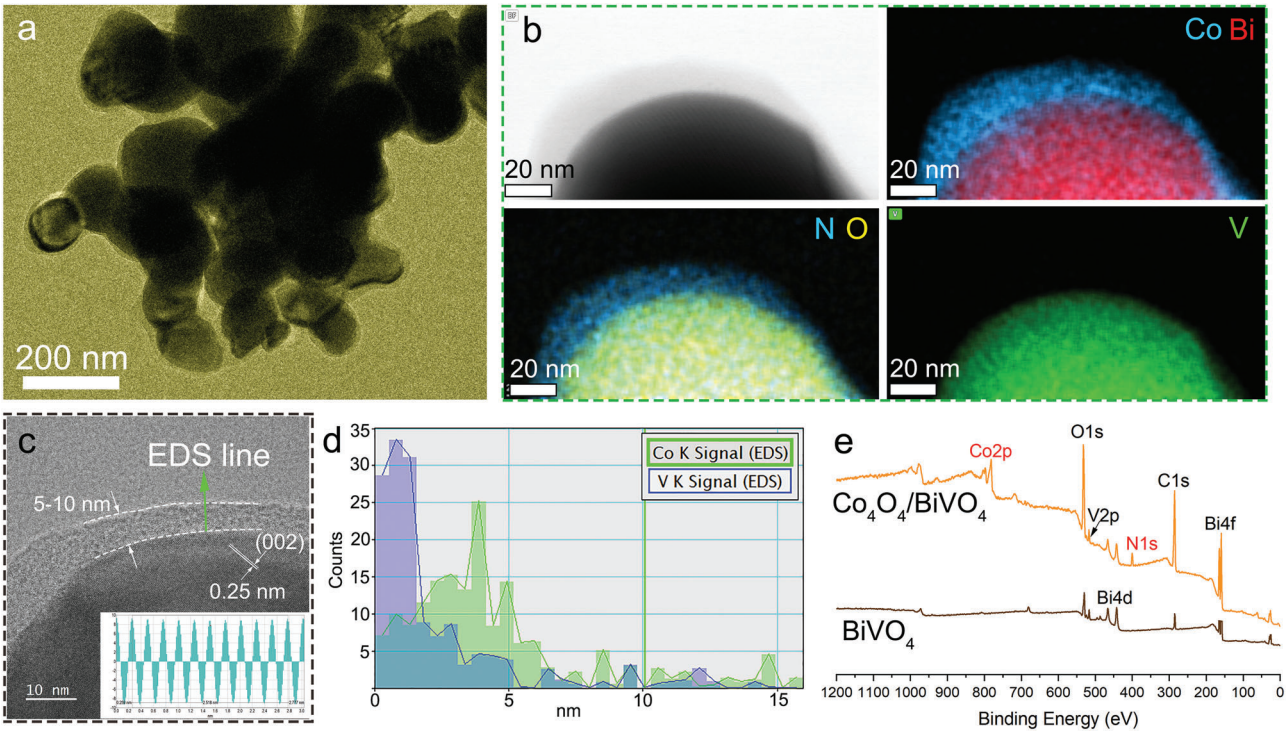

Figure 1. a) TEM image of $Co_4O_4/BiVO_4$ (BL12), b) bright-field scanning TEM images of $Co_4O_4/BiVO_4$ (BL12) with corresponding EDX elemental mappings, c) high-resolution TEM images showing lattice fringe patterns, d) EDX line-scan profiles of $Co_4O_4/BiVO_4$, e) XP survey spectra of $Co_4O_4/BiVO_4$ and $BiVO_4$.

To further confirm that the cubane maintains its molecular nature on $BiVO_4$, a mixture of cubane borate and PAA solution was drop-casted on FTO surface and examined with Raman spectroscopy. Raman spectra confirmed the integrity of the cubane structures, because the characteristic vibrational bands of the cubane and PAA mixtures on FTO are largely the same as that of Co_4O_4-dpk crystals, especially in the metal–ligand bond vibration (<500 cm^{-1}) (Figure S5, more details in the Supporting Information). Transmission electron microscopy (TEM) images showed the tuned thickness of the cubane layers from ≈2 to ≈60 nm by increasing the assembling cycles from 4 to 20, as depicted in Figures S6,S7 (Supporting Information). For a typical $Co_4O_4/BiVO_4$ film (BL12), a conformal layer with a thickness of ≈10 nm was obtained on the $BiVO_4$ surface (**Figure 1**a,c), and energy-dispersive X-ray (EDX) mapping confirmed the presence of homogeneously distributed cobalt centers in the layer (Figure 1b). As the cubane is distributed in the polymer matrix on a molecular level, XRD patterns cannot confirm the presence of the molecular cubane but verified the monoclinic phase of $BiVO_4$ (Figure S8, Supporting Information). Nonetheless, X-ray photoelectron spectroscopy (XPS) survey spectra showed the additional presence of cobalt and nitrogen in $Co_4O_4/BiVO_4$ with respect to the original $BiVO_4$ sample (Figure 1e). No obvious shifts of the Bi and V peaks were observed after loading of the cubane layer (Figures S2,S30, Supporting Information), highlighting that cubane layers did not modify the support underneath. The slight decrease in the vanadium peak intensity could be assigned to the shielding of the $BiVO_4$ surface from the X-ray beam by the cubane layer. Moreover, high-resolution X-ray photoelectron (XP) spectra recorded at the Co peak positions of $Co_4O_4/BiVO_4$ confirmed the presence of two major peaks at ≈781.8 eV (Co $2p_{3/2}$) and Co $2p_{1/2}$ (≈797.8 eV), corresponding to a spin-orbit splitting (ΔCo 2p = Co$2p_{1/2}$—$2p_{3/2}$) of 15.9 eV and an explicit satellite peak of Co(II) at ≈786.7 eV (Figure 6b).[36]

2.2. PEC Water Oxidation Driven by $Co_4O_4/BiVO_4$ Photoanodes

The PEC water oxidation performance of photoanodes was first evaluated by linear sweep voltammetry (LSV) under AM 1.5 G simulated solar irradiation at 100 mW cm^{-2} (**Figure 2**a; Figure S9, Supporting Information). The assembly of the cubane layer on $BiVO_4$ films dramatically improved the water oxidation photocurrent density. The bi-layer cycles of 10 and 12 delivered photocurrents of ≈3.3 mA cm^{-2} at 1.2 V versus RHE, ≈5 times more than that of pristine $BiVO_4$ films, as shown in Figure 2b. The trends of photocurrents resemble the normal distribution, which coincides with UV/vis results that $Co_4O_4/BiVO_4$ films of ≈12 bi-layers displayed maximum absorption with more photogenerated hole–electron pairs. The dark LSV currents of $BiVO_4$ and BL12, as well as the discrepancy between them, can both be neglected, as shown in Figure S10 (Supporting Information).

Moreover, the photocurrent density of BL12 further increased to 4.1 mA cm^{-2} in the presence of sulfite as a hole scavenger (Figure 2c), which is comparable to previously reported results.[22,34,35,37] As shown in Figure 2a,c, photocurrents were initiated at a significantly low potential of ≈0.15 V versus RHE

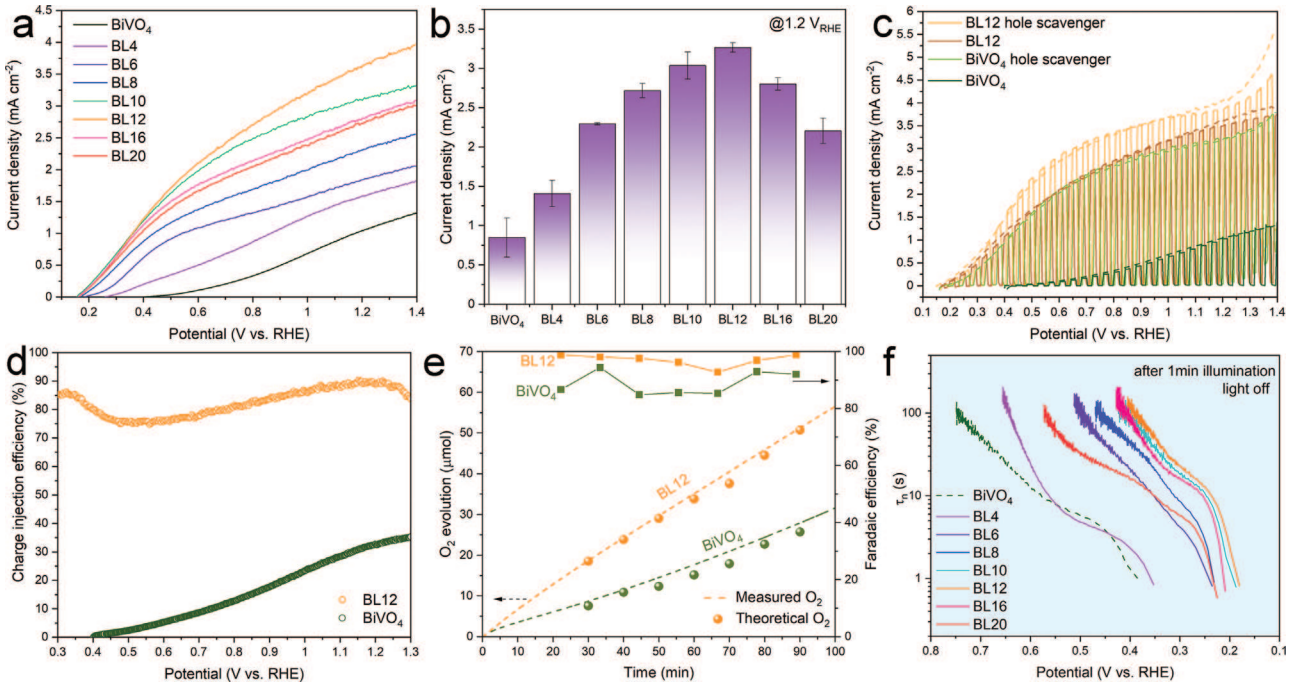

Figure 2. a) LSV curves of $BiVO_4$ and $Co_4O_4/BiVO_4$ assembled with different LBL bi-layers recorded at a scan rate of 20 mV s^{-1}, b) photocurrents at 1.2 V versus RHE obtained from Figure 2a and Figure S7 (Supporting Information), c) chopped LSV curves of $BiVO_4$ and BL12 measured in 1 M Na_2SO_3 solution (pH 9.7) as hole scavenger and 0.5 M borate buffer (pH 8), respectively, d) charge injection efficiency (η_{inj}) of $BiVO_4$ and BL12, obtained from Equation S1 (Supporting Information), e) Theoretical O_2 amount (dotted lines) calculated from the photocurrent assuming 100% Faradaic conversion efficiency and measured O_2 evolution amount (spheres) as well as Faradaic efficiencies (rectangles) of $BiVO_4$ and BL12 photoanodes at 1.23 V versus RHE under 1.5 sun illumination, f) charge carrier dynamics derived from OCP decay after light-off (τ_n: lifetime of photogenerated charge carriers). All films were measured in 0.5 M borate buffer (pH = 8) and under 1 sun illumination (AM 1.5 G, 100 mW cm^{-2}) in this study unless otherwise mentioned.

when more than six bilayers were applied, which is ≈320 mV lower than the onset potential of pristine $BiVO_4$. Obviously, the photocurrents at/below the onset potential of $BiVO_4$ were greatly enhanced by loading the cubane layer. Importantly, the cubane layer (BL12) greatly improved hole injection efficiency from 0 to ≈80% at ≈0.3–0.4 V versus RHE (Figure 2d), which indicates that more holes were saved from recombination and instead readily transferred to the OER.[27]

The incident photon to current efficiency (IPCE) measured at 1.23 V versus RHE (Figure S11a, Supporting Information) showed enhanced charge carrier collection near the band edge (460–525 nm) for $Co_4O_4/BiVO_4$ films. Moreover, the BL12 cubane films showed the highest IPCE with 80% photon to electron efficiency in the wavelength range from 350 to 460 nm, instead of 35% for $BiVO_4$. The theoretical photocurrent densities converted from the incident photons were obtained based on the standard AM 1.5 G solar spectrum. As the theoretical photocurrent limit of $BiVO_4$ is ≈7.5 mA cm^{-2} at 1 sun illumination,[38] the BL12 cubane films achieved ≈53% of the theoretical photocurrent density compared to ≈23% for $BiVO_4$ (Figure S11b, Supporting Information) when held at a bias of 1.23 V versus RHE. Although a mismatch is generally observed between the IPCE spectra and the absorption features of photoanodes,[39] the enhanced absorption by the cubane layer can still account for enhanced photocurrents, as more photons were absorbed and converted into photogenerated carriers. However, further increasing cubane layer thickness will hinder the absorption of $BiVO_4$ and the migration of holes to the surface, resulting in reduced photocurrents and IPCE.

The evolution of oxygen during the PEC process was confirmed by using a custom-built cell and gas chromatography, see Section 4 (Supporting Information). Due to the limited PEC performance of $BiVO_4$, both illumination area and intensity were increased to reduce the measurement errors of originally low oxygen amounts (Figure S12, Supporting Information). The GC results evidenced oxygen evolution (Figure S13, Supporting Information). Moreover, the measured oxygen quantities of both BL12 and $BiVO_4$ photoanodes increased linearly with time, fitting well with the theoretical oxygen amount converted from photocurrents assuming 100% Faradaic efficiency (Figure 2e). The Faradaic efficiency of BL12 is ≈100%, confirming the effective conversion of water to oxygen, while a slight loss of Faradaic efficiency was observed on $BiVO_4$ probably due to photocorrosion.[40]

To probe the band bending and dynamics of photogenerated charge carriers, open-circuit potential (OCP) measurements were conducted under chopped light conditions. After stabilizing the semiconductor electrode in electrolytes and in darkness, the Fermi levels of semiconductors and redox couples in the electrolyte will be in equilibrium through interfacial charge transfer, resulting in the bending of the band edges.[41] At the same time, the charged ions absorbed on the electrode surface generated an electric field in the dark, which established a potential between the working electrode and the environment (OCP_{dark}), with respect to a reference electrode. Upon illumination, the charge

carriers are generated and separated in the space charge region. The subsequent accumulation of minority charge carriers at the SEI generates a compensating electric field, leading to flattened band edges and reduced open circuit potential in light (OCP_{light}). The difference (ΔOCP) between OCP_{dark} and OCP_{light} was often regarded as the photovoltage.[42,43] However, for semiconductors in electrolytes, ΔOCP only reflects the change of the Fermi level, and it is affected by a wide range of non-ideal parameters, such as redox species in electrolytes, surface properties, recombination, defects, surface states, among others.[44] Nevertheless, it can still be deduced from Figure S14 (Supporting Information) that assembling a cubane layer on $BiVO_4$ changes the interfacial energetics and the Fermi level equilibrium as discussed above. Hence the negatively shifted OCP_{dark} of $Co_4O_4/BiVO_4$ reflects the reduction of band bending in the dark, and the loading of the cubane layer facilitated the generation of a compensating electric field in the space charge region, thereby improving charge separation and shifting photocurrent onset potentials to lower values. Additionally, the decay of the OCP_{dark} (Figure 2f) showed a prolonged lifetime of photogenerated charge carriers on cubane-modified films, pointing to suppressed recombination processes of photogenerated electron–hole pairs.

2.3. Kinetic Behavior Derived from Time-Dependent Perturbations

The water oxidation performance is fundamentally influenced by a series of kinetic processes ranging from ultrafast charge carrier generation and separation all the way to slow interfacial charge transfer and recombination.[45,46] It is essential to monitor the dynamics of photo-generated charge carriers from the generation in the space charge region to consumption in sluggish interfacial processes at longer timescales (μs–s) under reaction conditions. TPS measurements, as a more accessible technique than TAS, enable to show the dynamics of slow interfacial processes by analyzing the current response to a time-dependent perturbation in photon flux and bias (Figure S15, more details in, Section 6, Supporting Information). **Figure 3**a–d shows the transient photo-process under the perturbation of light and bias from 0.3 to 1.2 V versus RHE on $BiVO_4$ and $Co_4O_4/BiVO_4$ films with bi-layers ranging from 4 to 20, which were obtained from the second current-light response in the TPS curves (Figures S16–S23, Supporting Information). The anodic photocurrents of the cubane-modified photoelectrodes were increased 53-fold in the vicinity of the onset potential (≈0.3 V vs RHE). Moreover, the cathodic spikes were eventually suppressed in the higher potential region (>0.9 V vs RHE) for films with cubane layers of moderate thickness.

The decay behavior of charge carriers after light-off was proposed to represent the reduction or transfer of accumulated photo-holes in the form of oxidized intermediates that had survived on the surface.[47] Hence, the number of electrons was integrated over time, and the total amount of charge is summarized in Figure 3e. The sign of currents represents the direction of electron flow and fundamentally reflects whether surface holes are forward transferred to the electrolyte (positive) or backward recombined with conduction band electrons (negative). For $BiVO_4$ films, the significant cathodic spikes indicated that recombination was the predominant pathway for surface holes even at high potential. However, for $Co_4O_4/BiVO_4$ films with bi-layers approximately between 6 to 16, the preferred forward transfer was becoming the dominant process. An overload of cubanes (BL ≥ 16) eventually leads to the recurrence of the recombination pathway, as indicated by the negative cathodic spikes. Therefore, it can be concluded that moderate catalyst loading is better to direct the photogenerated holes toward the favorable charge transfer reaction, while an excessive amount of loading leads to the reduction of charge transfer in the inner layer, resulting in shifting the balance to the recombination side. Hole consumption in the dark can proceed via recombination with conduction band electrons, intermolecular coupling into inactive species (i.e., peroxides), and charge transfer to water. Thus, it can be deduced that the remaining holes stored in oxidized cubane molecules enable fast charge transfer to water even after light-off, giving rise to a prolonged positive current for a moderate thickness of the catalytic layer. However, the increased concentration of cubane molecules in the thick catalytic layer first strengthens the coulombic force attracting conduction electrons, then blocks hole transfer from $BiVO_4$ to cubane and water due to long transportation distances, and finally reinforces the intramolecular coupling of oxidized intermediates[48] into inactive species. These factors altogether contribute to the prevailing occurrence of cathodic recombination after light-off.

The kinetic process was further analyzed by comparing the rate constants of charge transfer (k_{ct}-TPS) and recombination (k_{rec}-TPS) processes, which were regarded as diagnostic parameters fitted from the anodic current decays under illumination (see Section 6, Supporting Information).[49] Transient photocurrent decays under illumination were also examined as a function of the potential and cubane layer thickness. First, the hole transfer efficiencies were greatly improved over a wide potential range, especially for $Co_4O_4/BiVO_4$ films with 8–12 bi-layers (Figure 3f). The transfer efficiency mapping is obtained from a pseudo-steady-state, and it can explain the difference of the *J–V* behavior of $Co_4O_4/BiVO_4$ films in Figure 2a. The thin cubane layer enhanced the charge transfer efficiency (Figure 3f), hence contributing to the increased currents at the negatively shifted onset potential region. For moderate layer thickness (BL10-12), the transfer efficiency reaches the maximum in all potential ranges, which coincides with their *J–V* behavior at the highest photocurrents (Figure 2a). Further, increasing layer thickness enhances the k_{ct}-TPS slightly at higher potential and k_{rec}-TPS largely at lower potential (Figure 3g,h), leading to a slight increase of photocurrents at higher potentials and less cathodic shift of the onset potential, respectively.

Moreover, cubane layers with moderate thickness (≈10–12 bi-layers) achieved the highest k_{ct}-TPS (0.14 s^{-1}) at 1.2 V versus RHE (Figure 3g), which is approximately three-fold higher than the value for pristine $BiVO_4$ electrodes (≈0.048 s^{-1}) at the same potential. Notably, cubane loading significantly reduced the value of k_{rec}-TPS from 0.34 s^{-1} for $BiVO_4$ to 0.0066 s^{-1} for BL12 at lower potentials (Figure 3h). However, thick layers (≈16–20 bi-layers) lead to a simultaneous increase of k_{ct}-TPS and k_{rec}-TPS at lower potentials. Through the above analysis, the role of cubane layers can be reasonably assigned as a passivation layer at lower potentials for thin/moderate thickness and as a catalytic layer at higher potentials for moderate thickness, respectively. For moderate

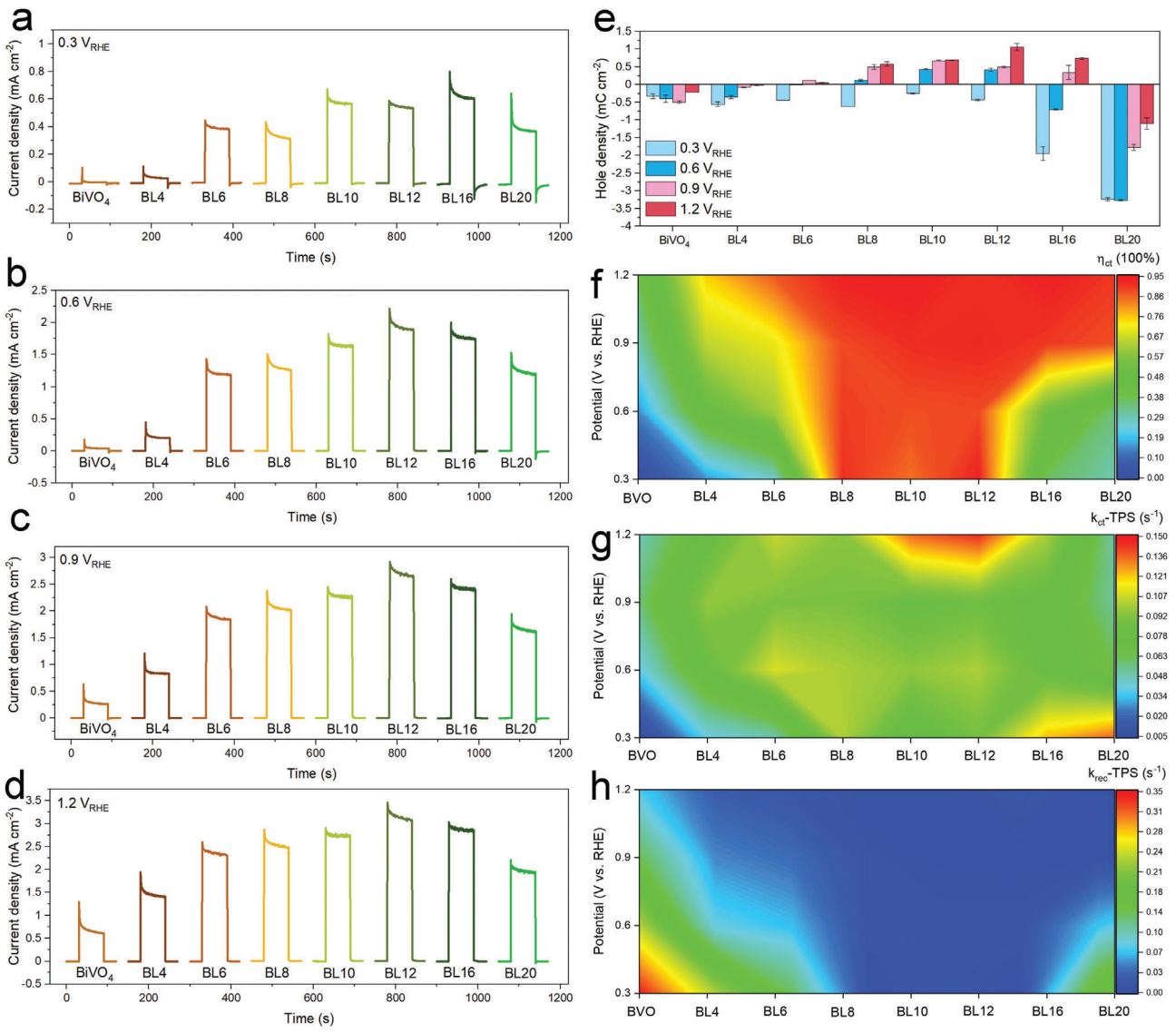

Figure 3. a–d) Transient current responses of $BiVO_4$ and $Co_4O_4/BiVO_4$ with different bi-layers obtained at applied potentials of 0.3/0.6/0.9/1.2 V versus RHE in 0.5 M borate buffer (pH 8.0), e) anodic and cathodic charge passed after light-off as a function of potentials, f–h) contour maps of hole transfer efficiency during illumination, charge transfer constant (k_{ct}-TPS), and recombination constant (k_{rec}-TPS) as a function of potentials and layer thicknesses. All films were measured under 1 sun illumination (AM 1.5 G, 100 mW cm^{-2}).

potentials, complementary techniques were further employed to understand the function of the cubane layer.

2.4. Kinetic Behavior Derived from Frequency-Dependent Perturbations

Two types of perturbation techniques, namely sinusoidal potential or illumination intensity modulation, were applied to study fundamental kinetic processes in the bulk semiconductor or at the SEI. A typical equivalent circuit representing the SEI junction was used to analyze the PEIS results (**Figure 4**e; Figure S24, Supporting Information), including space charge capacitance and resistance of the bulk $BiVO_4$, C_{bulk} and R_{bulk}; interface capacitance and resistance, C_{int} and R_{int}; and contacting resistance, R_s.[50]

In the Bode plots, the magnitude of the frequency reflects the time scale of kinetic processes involved in the OER, while the phase shifts in each characteristic frequency domain originate from the capacitive behavior of a given kinetic process with corresponding resistive-capacitive effects. The assignment of the time scale to specific charge transportation processes (charge generation, charge migration, surface charge trapping) has recently been reviewed by Durrant et al. using time-resolved TAS.[45] Specifically, it was found that a slow hole transfer from metal oxide to a surface-bound species, with a time scale of seconds, contributed to the slower kinetics of interfacial water oxidation. Besides the charge-carrier dynamics in the bulk were found to be faster than those on the surface. Here, two main peaks centered ≈0.7–3.4 and 15–50 Hz were observed on $BiVO_4$ and BL4 films at 0.3 V versus RHE, respectively. These peaks were assigned to

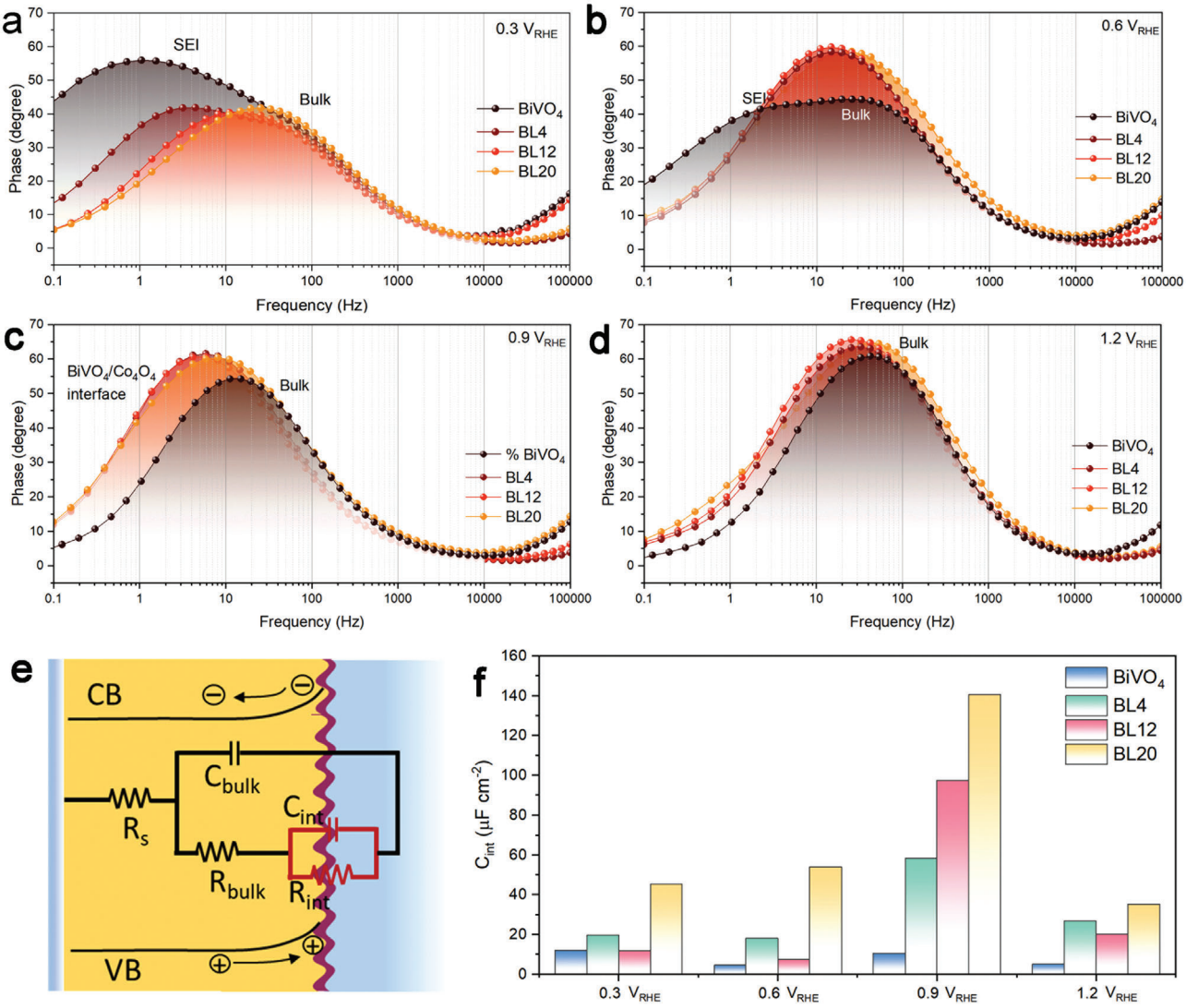

Figure 4. a–d) Bode plots of $BiVO_4$ and $Co_4O_4/BiVO_4$ films with 4/12/20 bi-layers obtained at different potentials: 0.3/0.6/0.9/1.2 V versus RHE, e) equivalent circuit for analyzing impedance data, f) interface capacitances fitted from Nyquist plots. To keep impedance measurements in a steady state and to avoid disturbance by oxygen bubbles, a blue light-emitting diode (LED) with a light intensity of 50 W m^{-2} and a wavelength of 476 nm was used for illumination.

the sluggish charge transfer processes at the SEI and to charge generation and transportation processes in bulk semiconductors for $BiVO_4$ and BL4 films (Figure 4a), based on the above analysis and their similar time domain characteristics. Especially for $BiVO_4$, the lowest frequency domain showed the highest phase shift, indicating that the charge transfer at the SEI was the main kinetic limitation. After increasing the bi-layer number to 12 or elevating the potential to 0.6 V versus RHE, the phase shift was reduced at the SEI domain but became predominant at the bulk domain (Figures 4a,b). This suggested that reaction kinetics were gradually limited by the bulk at higher potential, especially for $Co_4O_4/BiVO_4$ films.

Interestingly, at 0.9 V versus RHE, a new phase peak at 3.7–12.5 Hz, lower than the bulk domain of $BiVO_4$, was found in $Co_4O_4/BiVO_4$ films (Figure 4c). Similar charge transfer processes from $BiVO_4$ to the Ni(Fe)OOH cocatalyst layer were also found with a time scale of microseconds,[14] as well as the charge transfer process between a Fe_2O_3/NiOOH interface.[51] Therefore, it is reasonable to tentatively assign this frequency domain to a hole transfer process between $BiVO_4$ and the Co_4O_4 layer ($BiVO_4/Co_4O_4$ interface). This was confirmed by the dramatically increased C_{int} in all $Co_4O_4/BiVO_4$ films at 0.9 V versus RHE (Figure 4f), indicating that the oxidation of cubanes was activated with the increase of potential, resulting in the trapping of more holes in the cubane layer. These results revealed that the holes may undergo kinetic processes with slower consumption rates, leading to smaller slopes of LSV curves at moderate potential for thicker cubane layers.

At 1.2 V versus RHE, the oxygen evolution is mainly limited by the intrinsic properties of the semiconductor (driving force in the space charge region). Thus, the phase peaks for $BiVO_4$ and $Co_4O_4/BiVO_4$ films represented the bulk domain again, and both

moved back to a higher frequency. However, the frequency domain of $Co_4O_4/BiVO_4$ films is still lower than that of $BiVO_4$ due to the minor influence of slower hole-trapping processes in the cubane layer.

In general, C_{int} representing accumulated holes at the SEI is strongly correlated to the amount of cubane loading over a wide range of applied potentials, especially at 0.9 V versus RHE (Figure 4f). Moreover, as shown in Table S1 (Supporting Information), an interesting phenomenon of potential-dependent resistances was observed, namely that the Co_4O_4 layer reduced resistances significantly (especially for R_{int}) at lower potentials while possessing higher resistances than that of $BiVO_4$ at higher potentials. This is also the reason why the onset photocurrents of $BiVO_4$ films are greatly improved due to minimized transfer resistances. The slight increase of resistances at higher potentials can be attributed to more holes being trapped in the cubane layer, which also generates resistance to further transfer them to water.

On top of the above analysis, the cubane molecules in the layer primarily acted as hole scavengers at 0.9 V versus RHE, mediating charge transfer at the SEI, and then changing their role toward catalyst functionality at higher potentials.

On the other hand, charge transfer and surface recombination kinetics at the onset potential region were investigated by IMPS by modulating the concentration of the surface photo-generated carriers.[52] This technique offers a kinetic understanding of the surface at near steady-state, which is closer to an operando condition when compared with TPS obtained through time-dependent chopped-light perturbations.

To understand the surface carrier dynamics at the SEI, the reaction rate constants for charge transfer (k_{tr}) and surface recombination (k_{rec}) were extracted from Nyquist plots of IMPS (see Section 7.2, Supporting Information). For $BiVO_4$, the upper recombination semicircles are large and barely changed over the onset potential range (**Figure 5**a), which corresponds to high k_{rec} values (Figure 5f). After modification with a moderate amount of cubanes, k_{rec} was dramatically reduced, and k_{tr} was improved.

However, an excess amount of cubane loading (BL20) gave rise to i) higher k_{rec} at a potential of ≈0.2 to 0.3 V versus RHE and ii) much elevated k_{tr}, meanwhile milder suppressed k_{rec} at a potential of ≈0.35 to 0.45 V versus RHE, compared to BL12 and BL4 (Figure 5e,f). Overall, the BL20 photoelectrodes delivered notably enhanced performance compared to pristine $BiVO_4$ films but lower than optimized BL12. This points to the fact that both transfer constant and recombination constant are relevant values, while either of them alone is not able to predict the photocurrent output, as indicated by Equation (S11) (Supporting Information). As expected, the thick cubane layer not only contained more cubane molecules but also increased the charge transportation distance. At lower potentials (0.2 to 0.3 V vs RHE), the minor band bending in $BiVO_4$ cannot effectively drive holes to cubane molecules but leads to more recombination from closer packed cubane molecules with high-valent Co centers. Once the band bending is sufficient to drive hole transfer to cubane layers with appropriate thickness, the recombination can be significantly passivated, affording a higher k_{tr} (>0.35 V vs RHE). Therefore, the primary role of the Co_4O_4 layer is to passivate surface recombination (surface passivation) in the onset potential region (≤0.3 V vs RHE), especially for moderate layer thickness. This is also revealed by the TPS analysis showing enhanced charge transfer efficiency for moderate thickness and at lower potential as shown in Figure 3f. The above factors are accounting for a lower and positively shifted onset current in the *J–V* curves (Figure 2a).

2.5. PEC Stability of Photoanodes

As shown in **Figure 6**a and Figure S26 (Supporting Information), photocurrents decreased in the first 1.5 h for $Co_4O_4/BiVO_4$ photoanodes rather than slightly increasing as for bare $BiVO_4$ due to the photo-charging effect.[43] After that, the photocurrents of BL10/12 stabilized at ≈2 mA cm^{-2}, but the photocurrents of $BiVO_4$ gradually dropped to ≈0.5 mA cm^{-2}.

Stabilizing the $BiVO_4$ photoanodes can be achieved by effectively inhibiting the leaching of V^{5+} into the electrolyte. Techniques such as high-temperature treatment for films or the use of a V^{5+}-saturated electrolyte have shown promising results in this regard.[53] Hence, the metal ion concentrations (Bi/V/Co) in the electrolyte were determined using ICP-MS measurements after 22 h of PEC water splitting. After assembly of the cubane layer (BL10), the ICP-MS results (Table S2, Supporting Information) showed that the dissolution of Bi and V was reduced from 6.69 and 112.86 μg L^{-1} to ≈0 and 9.73 μg L^{-1}, respectively. Additionally, the leaching of Co in the electrolyte was found to be only 15.66 μg L^{-1}. Rather than Co leaching, the slight decrease of photocurrents of $Co_4O_4/BiVO_4$ could be attributed to more sophisticated reasons, arising from $BiVO_4$ itself or the transformations of $Co_4(II)O_4$ to $Co_4(III/IV)O_4$, Co molecular species, or cobalt oxides/oxyhydroxides/hydroxides under anodic bias for extended holding times. Therefore, STEM and XP spectroscopy were employed to investigate the surface for post-reaction changes. First, electron microscopy images in Figure S27 (Supporting Information) showed that the cubane layer of post-22 h was distorted by aging at 1.0 V versus RHE for 20 h. Nevertheless, no particular crystalline species were detected in the cubane layer, and Co species remained homogeneously distributed in the surface layer, as confirmed by STEM/EDX elemental mappings. XPS data recorded before and after aging enable to further characterize the changes occurring in the cubane layer. Co(II) can exclusively be identified in the high-resolution XPS spectra just after the LBL assembling process. Prolonged aging of $Co_4O_4/BiVO_4$ resulted in a weakening of the characteristic satellite peaks of Co(II) at 786.7 eV, and the appearance of a new peak at 780.6 eV together with a satellite peak at 789.9 eV that could be assigned to the appearance of Co(III) species, further highlighting the partial oxidation of the surface Co species after long-term illumination.

All in all, these results suggest that part of the surface $Co_4(II)O_4$ molecules may have undergone a transformation into other high-valent cobalt species after holding under anodic bias and illumination for long periods of time. Moreover, C═O and C—O groups were identified in O 1s and C 1s XP spectra after cubane loading (Figure 6c; Figure S28, Supporting Information), which confirmed the presence of PAA in $Co_4O_4/BiVO_4$ films. After aging the films for 22 h, an increased fraction of oxygen vacancies was furthermore found in $Co_4O_4/BiVO_4$ (post-22 h).

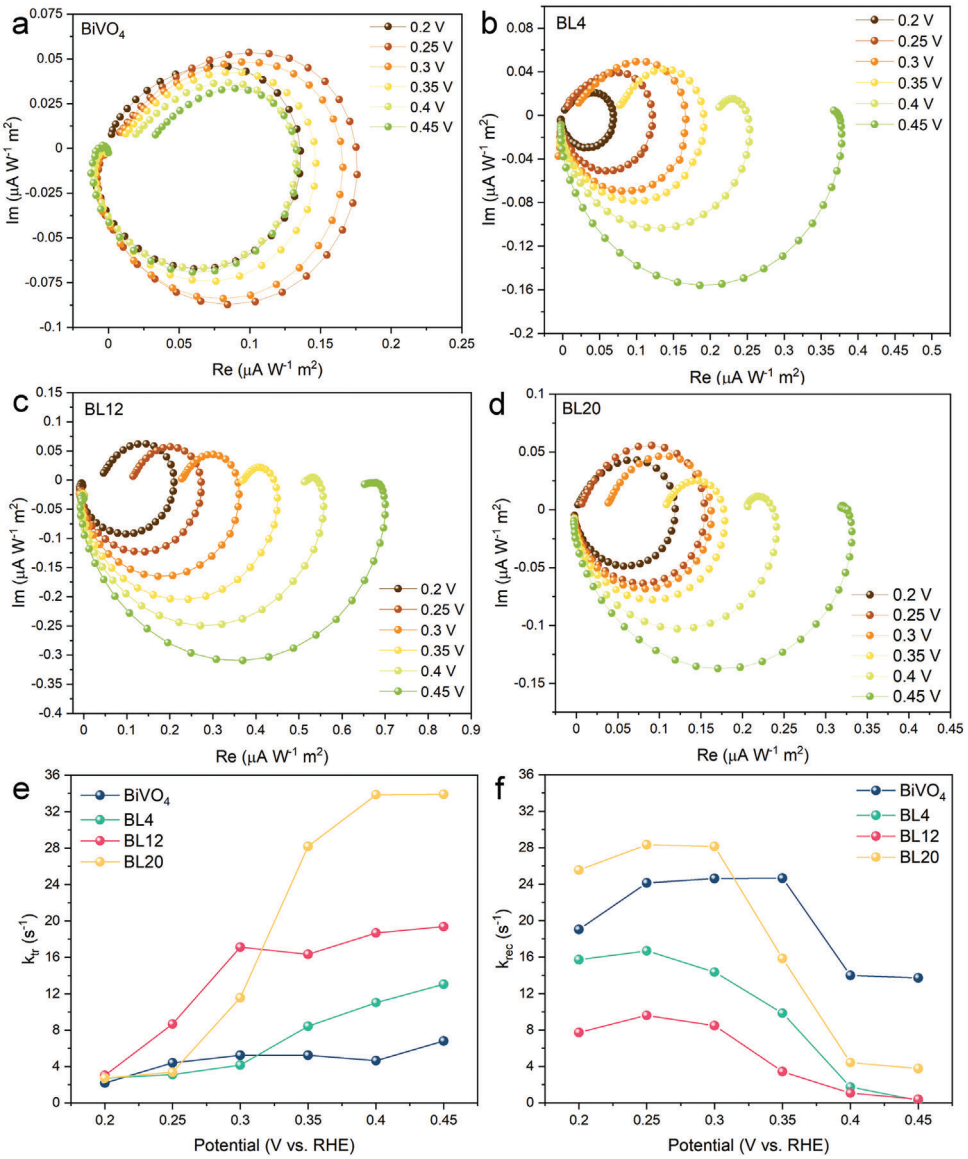

Figure 5. a–d) IMPS Nyquist plots of $BiVO_4$ and $Co_4O_4/BiVO_4$ films with 4/12/20 bi-layers obtained in onset potential region, e,f) rate constants (k_{tr} and k_{rec}) extracted from the IMPS data of $BiVO_4$ and $Co_4O_4/BiVO_4$ films at the onset potential region. A blue LED with a light intensity of 50 W m^{-2} and a wavelength of 476 nm was used for illumination.

2.6. Interpretation of the Role of Co_4O_4 Layers

Based on the above kinetic analysis, our understanding of the charge transportation process and the role of Co_4O_4 layers on $BiVO_4$ is summarized in **Scheme 1**. Previous studies reported that photo-generated holes accumulated on the surface and formed intermediate states at certain energetic levels to mediate water oxidation, such as for hematite and $BiVO_4$.[2,54] Thus, a localized peak is shown in Scheme 1 to represent intermediate states on $BiVO_4$. For $BiVO_4$, the accumulated holes were reported to participate in water oxidation but were mainly consumed by surface recombination as a widely recognized loss pathway.[7] For thin Co_4O_4 layers, surface recombination was passivated to a large extent and the photocurrents were improved greatly, as shown in Figures 2a and 3h. This can be reasonably explained by the hypothesis that holes can possibly tunnel through thin layers via an outer sphere mechanism to oxidize water as widely proposed.[55] For moderate cubane loading layers, more $Co^{II}{}_4O_4$ cubane molecules participated in water oxidation and hence led to enhanced photocurrents. Therefore, the cubane layer was considered to serve as a passivation layer for lower thickness and as a catalytic layer for thick layers with higher cubane loading.

Previous studies reported that the $Co_4(II)O_4$ core is active for photo-driven water oxidation but underwent oxidation to Co(III/IV) during oxygen evolution with a slow recovery rate to Co(II).[33] Here, kinetic analyses further confirmed that i) at lower bias, the cubane layer mainly acts as passivation layer, and most Co(II) centers can be recovered; ii) at moderate bias, holes from $BiVO_4$ were easily trapped by cubanes through the oxidation of Co(II) to Co(III/IV), which was evidenced by the dramatic

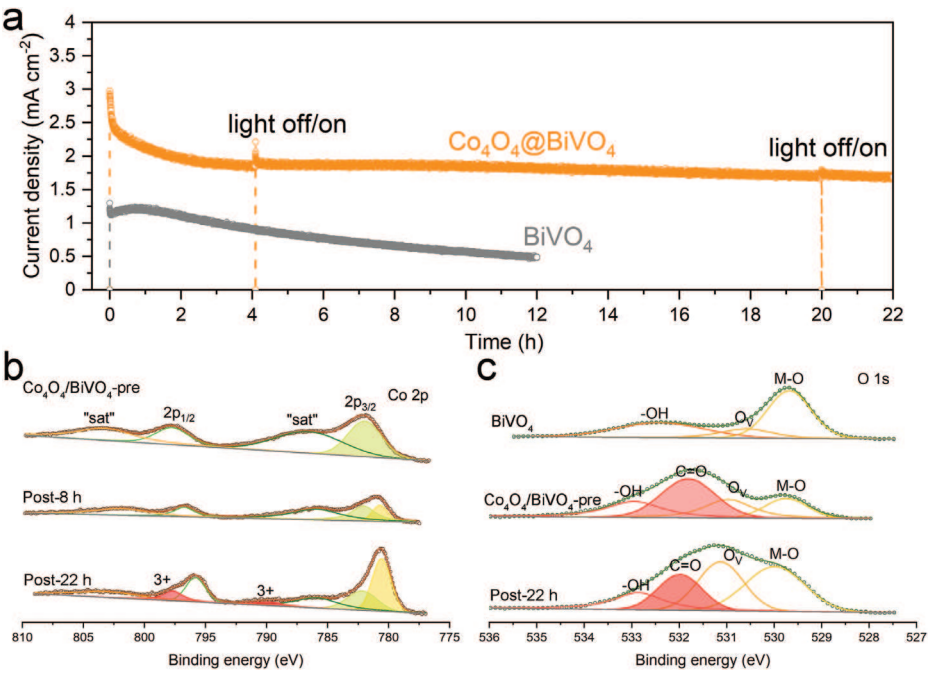

Figure 6. a) *J–t* plots of $BiVO_4$ and Co_4O_4/$BiVO_4$ (BL10) photoanodes at 1.0 V versus RHE for 22 h. b) High-resolution Co 2p XP spectra of Co_4O_4/$BiVO_4$ (BL12) photoanodes before catalytic tests (Co_4O_4/$BiVO_4$-pre), Co_4O_4/$BiVO_4$ (BL12) after tests (post-8 h), and Co_4O_4/$BiVO_4$ (BL10) after tests (post-22 h), c) high-resolution O 1s XP spectra of $BiVO_4$, Co_4O_4/$BiVO_4$-pre, and post-22 h. All films were measured under 1 sun illumination (AM 1.5 G, 100 mW cm^{-2}).

increase of interface capacitance, especially for thicker layers entrapping more Co_4(II)O_4 molecules; iii) under elevated bias, it was inferred that Co_4(III/IV) centers played the main role in water oxidation as active sites. According to our XPS results, the presence of Co(III) species after stability tests at moderate potentials also indicates that high-valent state Co centers are most probably involved in the OER process, but an explicit identification of Co(IV) valence states remains generally challenging.

3. Conclusion

This study presents a new approach to immobilize Co_4O_4 cubane on $BiVO_4$ photoanodes. These molecular cocatalysts are uniformly distributed on the $BiVO_4$ surface and delivered a superior PEC performance compared to most reported molecular-loaded photoanodes, as shown in Table S3 (Supporting Information). Optimization of the cubane layer thickness (10–12 BL) afforded the highest photocurrents of approximately 3.3 mA cm^{-2} at 1.23 V versus RHE, a ≈320 mV cathodic shift of the current onset potential, and prolonged stability with a photocurrent of ≈2 mA cm^{-2} maintained for at least 20 h. High hole injection efficiency, IPCE, and Faradaic efficiency identified Co_4O_4/$BiVO_4$ films as efficient water oxidation electrodes. A prolonged lifetime of photogenerated charge carriers and suppressed recombination processes were observed for Co_4O_4/$BiVO_4$ films through dynamic OCP decay studies. XPS results revealed that the cobalt valence state in the loaded cubane molecules remains +2 after short-time stability tests (≈8 h), while Co_4(II)O_4 molecules were partially transformed into Co(III) species and remained in their active post-catalytic states after long-time stability tests.

Most importantly, the kinetic behavior of photogenerated charge carriers was investigated in quasi-operando or steady-state conditions through a comprehensive set of PEC techniques. First, TPS results confirmed that the role of the cubane layer can be reasonably assigned as a passivation layer at lower potentials for thin/moderate thicknesses and as a catalytic layer at higher potentials for moderate thickness of the cubane layer, respectively. Further, the results of frequency-dependent PEIS under perturbed potentials revealed that the charge transfer domain varies as a function of applied potential and layer thickness. Charge transfer processes were dominant i) at the SEI for $BiVO_4$ at a potential below 0.6 V versus RHE and for Co_4O_4/$BiVO_4$ with a thin layer at 0.3 V versus RHE, ii) in the bulk for $BiVO_4$ at potentials above 0.6 V versus RHE and for Co_4O_4/$BiVO_4$ at 0.6 and 1.2 V versus RHE, iii) at the $BiVO_4$/Co_4O_4 interface for Co_4O_4/$BiVO_4$ at 0.9 V versus RHE. Moreover, the cubane layer was identified as the hole scavenger at 0.9 V versus RHE, thus mediating charge transfer at the SEI. Additionally, IMPS analysis which modulates surface hole densities revealed that Co_4O_4 layers greatly passivate the surface recombination at the onset potential region (≤0.3 V vs RHE) for moderate layer thicknesses, resulting in high hole injection efficiency at the onset potential.

All in all, our study opens up new avenues to stabilize molecular catalysts on photoanodes for enhanced performance in water splitting and energy conversion processes. We pioneered the comprehensive use of (photo)electrochemistry techniques based on time/frequency-dependent perturbations to fully resolve the complex role of cocatalysts in the context of varied conditions. This approach promotes photoelectrode design with new, efficient hybrid systems.

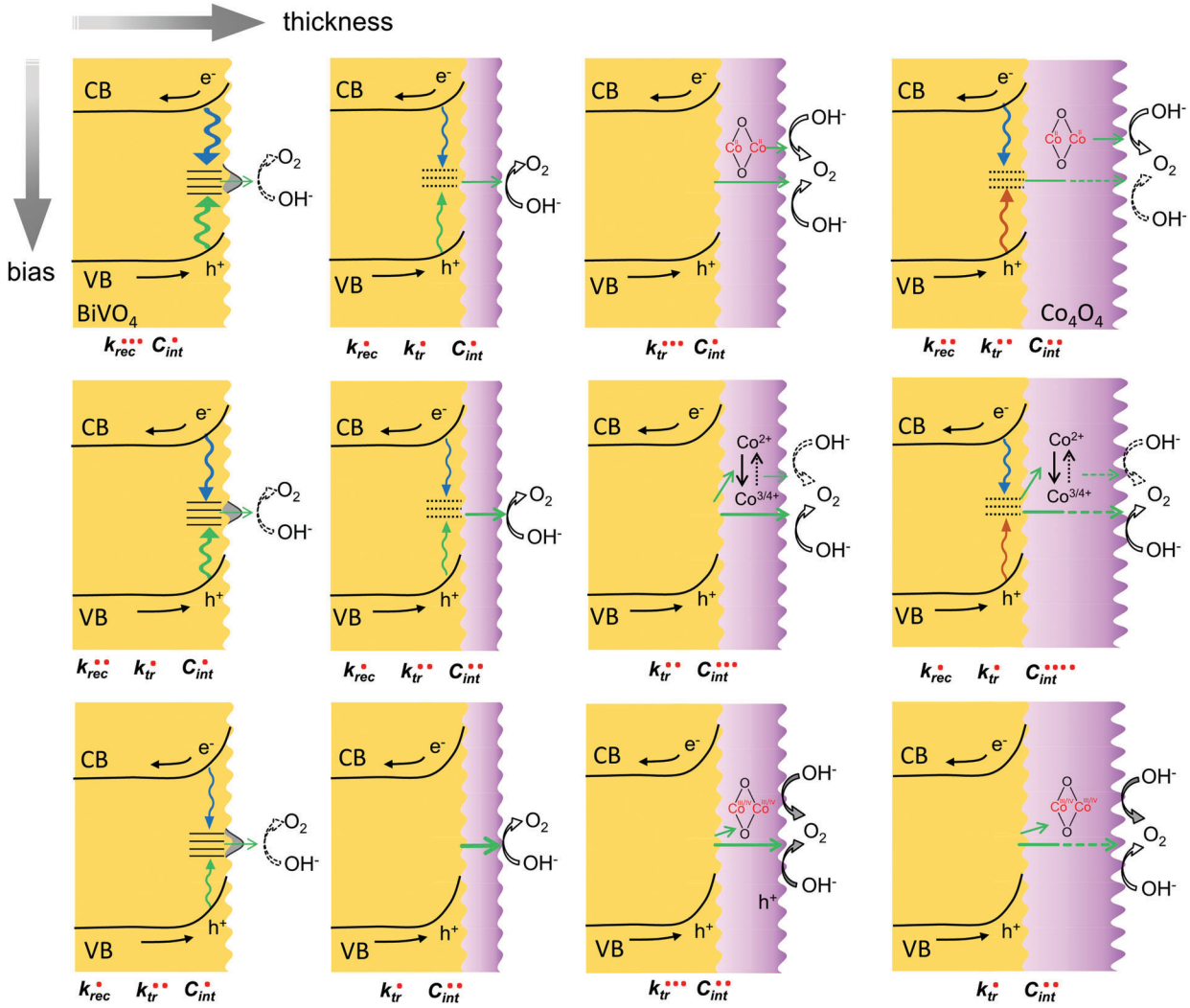

Scheme 1. Simplified models of the charge transport processes in $BiVO_4$ and $Co_4O_4/BiVO_4$ photoanodes as a function of the layer thickness and potential.

Supporting Information

Supporting Information is available from the Wiley Online Library or from the author.

Acknowledgements

This work was supported by the University Research Priority Program (URPP) for Solar Light to Chemical Energy Conversion (LightChEC). C.H. thanks the China Scholarship Council (CSC) for supporting her Ph.D. fellowship. The authors are grateful to Nicola Lüdi, Ying Kong, and Menglong Liu (University of Berne) for ICP-MS measurements.
Open access funding provided by Universitat Zurich.

Conflict of Interest

The authors declare no conflict of interest.

Data Availability Statement

The data that support the findings of this study are available from the corresponding author upon reasonable request.

Keywords

charge transfer processes, electrochemical impedance, layer-by-layer assembly, molecular catalysts, PEC water oxidation, photoanodes

Received: July 11, 2023
Revised: July 31, 2023
Published online: September 3, 2023

[1] a) P. Bornoz, F. F. Abdi, S. D. Tilley, B. Dam, R. van de Krol, M. Graetzel, K. Sivula, *J. Phys. Chem. C* **2014**, *118*, 16959; b) W. Yang, J. H. Kim, O. S. Hutter, L. J. Phillips, J. Tan, J. Park, H. Lee, J. D. Major, J. S. Lee, J. Moon, *Nat. Commun.* **2020**, *11*, 861.

[2] C. A. Mesa, L. Francàs, K. R. Yang, P. Garrido-Barros, E. Pastor, Y. Ma, A. Kafizas, T. E. Rosser, M. T. Mayer, E. Reisner, M. Grätzel, V. S. Batista, J. R. Durrant, *Nat. Chem.* **2020**, *12*, 82.
[3] a) B. Lamm, B. J. Trześniewski, H. Döscher, W. A. Smith, M. Stefik, *ACS Energy Lett.* **2018**, *3*, 112; b) T. W. Kim, K.-S. Choi, *Science* **2014**, *343*, 990; c) F. F. Abdi, L. Han, A. H. M. Smets, M. Zeman, B. Dam, R. van de Krol, *Nat. Commun.* **2013**, *4*, 2195.
[4] A. Kudo, K. Ueda, H. Kato, I. Mikami, *Catal. Lett.* **1998**, *53*, 229.
[5] J. K. Cooper, S. Gul, F. M. Toma, L.e Chen, P.-A. Glans, J. Guo, J. W. Ager, J. Yano, I. D. Sharp, *Chem. Mater.* **2014**, *26*, 5365.
[6] F. F. Abdi, T. J. Savenije, M. M. May, B. Dam, R. van de Krol, *J. Phys. Chem. Lett.* **2013**, *4*, 2752.
[7] C. Zachäus, F. F. Abdi, L. M. Peter, R. van de Krol, *Chem. Sci.* **2017**, *8*, 3712.
[8] Y. Lu, Y. Yang, X. Fan, Y. Li, D. Zhou, B. Cai, L. Wang, K. Fan, K. Zhang, *Adv. Mater.* **2022**, *34*, 2108178.
[9] D. K. Zhong, S. Choi, D. R. Gamelin, *J. Am. Chem. Soc.* **2011**, *133*, 18370.
[10] Z. Tian, P. Zhang, P. Qin, D.u Sun, S. Zhang, X. Guo, W. Zhao, D. Zhao, F. Huang, *Adv. Energy Mater.* **2019**, *9*, 1901287.
[11] a) J. Jian, S. Wang, Q. Ye, F. Li, G. Su, W. Liu, C. Qu, F. Liu, C. Li, L. Jia, et al., *Adv. Mater.* **2022**, *34*, 2201140; b) W. Yang, T. Moehl, E. Service, S. D. Tilley, *Adv. Energy Mater.* **2021**, *11*, 2003569.
[12] a) F. Yu, F. Li, T. Yao, J. Du, Y. Liang, Y. Wang, H. Han, L. Sun, *ACS Catal.* **2017**, *7*, 1868; b) Y. Ma, A. Kafizas, S. R. Pendlebury, F. L.e Formal, J. R. Durrant, *Adv. Funct. Mater.* **2016**, *26*, 4951.
[13] B. Klahr, S. Gimenez, F. Fabregat-Santiago, J. Bisquert, T. W. Hamann, *J. Am. Chem. Soc.* **2012**, *134*, 16693.
[14] L. Francàs, S. Selim, S. Corby, D. Lee, C. A. Mesa, E. Pastor, K.-S. Choi, J. R. Durrant, *Chem. Sci.* **2021**, *12*, 7442.
[15] F. S. Hegner, I. Herraiz-Cardona, D. Cardenas-Morcoso, N. López, J.-R. Galán-Mascarós, S. Gimenez, *ACS Appl. Mater. Interfaces* **2017**, *9*, 37671.
[16] B. Moss, F. S. Hegner, S. Corby, S. Selim, L. Francàs, N. López, S. Giménez, J.-R. Galán-Mascarós, J. R. Durrant, *ACS Energy Lett.* **2019**, *4*, 337.
[17] R. Matheu, P. Garrido-Barros, M. Gil-Sepulcre, M. Z. Ertem, X. Sala, C. Gimbert-Suriñach, A. Llobet, *Nat. Rev. Chem.* **2019**, *3*, 331.
[18] a) L. Duan, L. Tong, Y. Xu, L. Sun, *Energy Environ. Sci.* **2011**, *4*, 3296; b) X. Liang, X. Cao, W. Sun, Y. Ding, *ChemCatChem* **2019**, *11*, 6190; c) H.-Y. Liu, C. C. Cody, J. A. Jacob-Dolan, R. H. Crabtree, G. W. Brudvig, *ACS Energy Lett.* **2020**, *5*, 3195.
[19] Y. Wang, F. Li, X. Zhou, F. Yu, J. Du, L. Bai, L. Sun, *Angew. Chem.* **2017**, *56*, 6911.
[20] B. Zhang, F. Li, F. Yu, X. Wang, X. Zhou, H. Li, Y. Jiang, L. Sun, *ACS Catal.* **2014**, *4*, 804.
[21] J. Li, W. Wan, C. A. Triana, Z. Novotny, J. Osterwalder, R. Erni, G. R. Patzke, *J. Am. Chem. Soc.* **2019**, *141*, 12839.
[22] W. Jiang, X. Yang, F. Li, Q. Zhang, S. Li, H. Tong, Y. Jiang, L. Xia, *Chem. Commun.* **2019**, *55*, 1414.
[23] K. Fan, F. Li, L. Wang, Q. Daniel, H. Chen, E. Gabrielsson, J. Sun, L. Sun, *ChemSusChem* **2015**, *8*, 3242.
[24] C. Xu, W. Sun, Y. Dong, C. Dong, Q. Hu, B. Ma, Y. Ding, *J. Mater. Chem. A* **2020**, *8*, 4062.
[25] a) J. J. Richardson, M. Björnmalm, F. Caruso, *Science* **2015**, *348*, zaaa249411; b) G. Decher, M. Eckle, J. Schmitt, B. Struth, *Curr. Opin. Colloid Interface Sci.* **1998**, *3*, 32; c) T. Lee, S. H. Min, M. Gu, Y. K. Jung, W. Lee, J. U. Lee, D. G. Seong, B.-S. Kim, *Chem. Mater.* **2015**, *27*, 3785.
[26] J. Borges, J. F. Mano, *Chem. Rev.* **2014**, *114*, 8883.
[27] S. Bae, D. Kim, H. Kim, M. Gu, J. Ryu, B.-S. Kim, *Adv. Funct. Mater.* **2020**, *30*, 1908492.
[28] a) H. Kim, Y. You, D. Kang, D. Jeon, S. Bae, Y. Shin, J. Lee, J. Lee, J. Ryu, *Adv. Funct. Mater.* **2019**, *29*, 1906407; b) Y. Choi, D. Jeon, Y. Choi, D. Kim, N. Kim, M. Gu, S. Bae, T. Lee, H.-W. Lee, B.-S. Kim, J. Ryu, *ACS Nano* **2019**, *13*, 467.
[29] O. Shekhah, H. Wang, T. Strunskus, P. Cyganik, D. Zacher, R. Fischer, C. Wöll, *Langmuir* **2007**, *23*, 7440.
[30] F.-X. Xiao, J. Miao, B. Liu, *J. Am. Chem. Soc.* **2014**, *136*, 1559.
[31] C. Zhang, C. Chen, H. Dong, J.-R. Shen, H. Dau, J. Zhao, *Science* **2015**, *348*, 690.
[32] a) R. Brimblecombe, G. F. Swiegers, G. C. Dismukes, L. Spiccia, *Angew. Chem.* **2008**, *120*, 7445; b) C. G. Efthymiou, C. P. Raptopoulou, A. Terzis, R. Boča, M. Korabic, J. Mrozinski, S. P. Perlepes, E. G. Bakalbassis, *Eur. J. Inorg. Chem.* **2006**, *2006*, 2236; c) N. S. McCool, D. M. Robinson, J. E. Sheats, G. C. Dismukes, *J. Am. Chem. Soc.* **2011**, *133*, 11446.
[33] F. Song, R. Moré, M. Schilling, G. Smolentsev, N. Azzaroli, T. Fox, S. Luber, G. R. Patzke, *J. Am. Chem. Soc.* **2017**, *139*, 14198.
[34] B. Gao, T. Wang, X. Fan, H. Gong, P. Li, Y. Feng, X. Huang, J. He, J. Ye, *J. Mater. Chem. A* **2019**, *7*, 278.
[35] B. Gao, T. Wang, Y. Li, X. Fan, H. Gong, C. Jiang, P. Li, X. Huang, J. He, *Chem. Commun.* **2020**, *56*, 4244.
[36] J. Han, Y. J. Sa, Y. Shim, M. Choi, N. Park, S. H. Joo, S. Park, *Angew. Chem.* **2015**, *54*, 12622.
[37] S. Ye, C. Ding, R. Chen, F. Fan, P. Fu, H. Yin, X. Wang, Z. Wang, P. Du, C. Li, *J. Am. Chem. Soc.* **2018**, *140*, 3250.
[38] J. H. Kim, J. S. Lee, *Adv. Mater.* **2019**, *31*, 1806938.
[39] Z. Huang, Y. Lin, X. Xiang, W. Rodríguez-Córdoba, K. J. McDonald, K. S. Hagen, K.-S. Choi, B. S. Brunschwig, D. G. Musaev, C. L. Hill, D. Wangb, T. Lian, *Energy Environ. Sci.* **2012**, *5*, 8923.
[40] K. J. McDonald, K.-S. Choi, *Energy Environ. Sci.* **2012**, *5*, 8553.
[41] R. Krol in, *Electronic Materials: Science & Technology* (Eds.: R. van de Krol, M. Grätzel), Springer US, Boston, MA, **2012**, pp. 13–67.
[42] J. Xiao, L. Fan, F. Zhao, Z. Huang, S.-F. Zhou, G. Zhan, *J. Catal.* **2020**, *381*, 139.
[43] B. J. Trześniewski, W. A. Smith, *J. Mater. Chem. A* **2016**, *4*, 2919.
[44] S. P. Berglund, F. F. Abdi, P. Bogdanoff, A. Chemseddine, D. Friedrich, R. van de Krol, *Chem. Mater.* **2016**, *28*, 4231.
[45] S. Corby, R. R. Rao, L. Steier, J. R. Durrant, *Nat. Rev. Mater.* **2021**, *6*, 1136.
[46] S. Selim, E. Pastor, M. García-Tecedor, M. R. Morris, L. Francàs, M. Sachs, B. Moss, S. Corby, C. A. Mesa, S. Gimenez, A. Kafizas, A. A. Bakulin, J. R. Durrant, *J. Am. Chem. Soc.* **2019**, *141*, 18791.
[47] B. Klahr, S. Gimenez, F. Fabregat-Santiago, J. Bisquert, T. W. Hamann, *Energy Environ. Sci.* **2012**, *5*, 7626.
[48] K. M. H. Young, B. M. Klahr, O. Zandi, T. W. Hamann, *Catal. Sci. Technol.* **2013**, *3*, 1660.
[49] a) L. M. Peter, *J. Solid State Electrochem.* **2013**, *17*, 315; b) L. M. P., Gurudayal, L. H. Wong, F. F. Abdi, *ACS Appl. Mater. Interfaces* **2017**, *9*, 41265.
[50] S. Bae, H. Kim, D. Jeon, J. Ryu, *ACS Appl. Mater. Interfaces* **2019**, *11*, 7990.
[51] F. Malara, A. Minguzzi, M. Marelli, S. Morandi, R. Psaro, V. Dal Santo, A. Naldoni, *ACS Catal.* **2015**, *5*, 5292.
[52] a) Y. Liu, F. L.e Formal, F. Boudoire, N. Guijarro, *ACS Appl. Energy Mater.* **2019**, *2*, 6825; b) E. A. Ponomarev, L. M. Peter, *J. Electroanal. Chem.* **1995**, *396*, 219; c) D. Klotz, D. S. Ellis, H. Dotan, A. Rothschild, *Phys. Chem. Chem. Phys.* **2016**, *18*, 23438.
[53] a) Y. Kuang, Q. Jia, G. Ma, T. Hisatomi, T. Minegishi, H. Nishiyama, M. Nakabayashi, N. Shibata, T. Yamada, A. Kudo, et al., *Nat. Energy* **2017**, *2*, 15729; b) D. K. Lee, K.-S. Choi, *Nat. Energy* **2018**, *3*, 53.
[54] a) Q. Shi, S. Murcia-López, P. Tang, C. Flox, J. R. Morante, Z. Bian, H. Wang, T. Andreu, *ACS Catal.* **2018**, *8*, 3331; b) J. Li, W. Wan, C. A. Triana, H. Chen, Y. Zhao, C. K. Mavrokefalos, G. R. Patzke, *Nat. Commun.* **2021**, *12*, 255; c) H. Chen, J. Li, W. Yang, S. E. Balaghi, C. A. Triana, C. K. Mavrokefalos, G. R. Patzke, *ACS Catal.* **2021**, *11*, 7637.
[55] a) Y. W. Chen, J. D. Prange, S. Dühnen, Y. Park, M. Gunji, C. E. D. Chidsey, P. C. McIntyre, *Nat. Mater.* **2011**, *10*, 539; b) T. Moehl, J. Suh, L. Sévery, R. Wick-Joliat, S. D. Tilley, *ACS Appl. Mater. Interfaces* **2017**, *9*, 43614.